Applied Catalysis B: Environmental 244 (2019) 76–86

Contents lists available at ScienceDirect

Applied Catalysis B: Environmental

journal homepage: www.elsevier.com/locate/apcatb

Construction of Z-scheme $MoSe_2$/CdSe hollow nanostructure with enhanced full spectrum photocatalytic activity

Ying Wang[a], Jingxiang Zhao[a], Zhe Chen[a], Feng Zhang[a], Wei Guo[a], Huiming Lin[a,b,*], Fengyu Qu[a,b,*]

[a] Key Laboratory of Photochemical Biomaterials and Energy Storage Materials, Heilongjiang Province and College of Chemistry and Chemical Engineering, Harbin Normal University, Harbin, 150025, PR China

[b] Laboratory for Photon and Electronic Bandgap Materials, Ministry of Education, Harbin Normal University, Harbin 150025, PR China

ARTICLE INFO

Keywords:
Hollow $MoSe_2$/CdSe nanospheres
Z-scheme
Full spectrum photocatalysis
Cr(VI) photoreduction
Water splitting

ABSTRACT

For better use of solar energy, the development of full-spectrum photocatalysts has attracted most attentions. In this research, uniform hollow $MoSe_2$/CdSe nanospheres (250 nm) were prepared by one-pot solvothermal strategy. It is the first time to synthesize hollow $MoSe_2$ based nanostructure without any template/surfactant assistance. By varying reaction time, the formation mechanism was investigated, illuminating that the novel hollow structure is derived from the Kirkendall Effect. Both experimental and density functional theory (DFT) calculations reveal the Z-scheme mechanism of the charge transfer in the heterostructure. The hollow $MoSe_2$/CdSe nanospheres (MC2) possess the remarkable photocatalytic activity in degradation of Cr(VI) (125 mg g^{-1}, simulated sunlight), owing to the high harvest of full spectrum, porous hollow structure and effective charge separation/transfer. Furthermore, the photocatalytic process was further studied in detail, showing that the Langmuir single-layer adsorption behavior, low pH value condition, and thermal effect also benefit to the high photoreduction performance. Benefiting from the Z-scheme mechanism, the high redox activity make sure the water splitting capacity of MC2 (7120.0 and 348.0 μmol h^{-1} g^{-1} of H_2 and O_2 evolution) under simulated sunlight irradiation and its AQY for H_2 evolution at 670 nm reaches up to 27.2% (50 mg MC2).

1. Introduction

Today, the worldwide energy crisis and environmental pollution have become the grim challenge of human existence. Photocatalysis has been considered as one of the most potential ways to overcome these problems. However, the studies of photocatalysis have focused mostly on UV and visible lights, whereas the near-infrared (NIR) light which possesses nearly ~54% in the solar spectrum has been rarely harvest [1–4]. Over the past years, the searches of NIR light photocatalysts have focused mainly on upconversion luminescence of rare earth materials. The up-conversion materials can convert NIR excitation light into UV or visible emission to trigger photocatalysts, nevertheless, the low quantum efficiency further limited their further application. There is still a challenge to exploit efficient photocatalyst with broad spectrum harvesting of solar light, especially the NIR wavelength [5].

$MoSe_2$, a typical two-dimensional (2D) lamellar crystal, possesses narrow band-gap (1.33–1.72 eV) [5,6] to allow extending the acting light to NIR region. In addition, $MoSe_2$ possesses very high anti-photocorrosion stability due to the fact that the optical transitions are between nonbonding metal d states [7,8]. These characteristics make $MoSe_2$ as potential candidate in whole spectrum photocatalytic applications, such as decontamination, hydrogen production from water splitting, and photoelectronchemical solar cells, etc. For instance, Chu et al. demonstrated the $MoSe_2$ nanoparticles as a photocatalyst for degradation of Cr(VI) under UV–vis-NIR irradiation [9–11]. Few layer 1T-$MoSe_2$ was prepared and has been employed for the visible-light induced generation of hydrogen by Gupta et al. [12]. Dai synthesized novel $MoSe_2$ hierarchical microspheres for applications in visible-light-driven destroying organic pollutants [13].

In order to further improve their photocatalytic efficiency, the construct of heterostructure is an efficient way by reducing the recombination of photogenerated electron-hole pairs and promoting the charge transfer. In literature, some carbon materials (graphene oxide [14–16], C nanofibers [17,18], C cloth [19], and CQDs [20]) and other semiconductors (NiSe [21], WSe_2 [22], $ZnIn_2S_4$ [23], HfS_2 [24] and $CaIn_2S_4$ [25]) were mostly adopted to associate with $MoSe_2$

* Correspinding authors at: Key Laboratory of Photochemical Biomaterials and Energy Storage Materials, Heilongjiang Province and College of Chemistry and Chemical Engineering, Harbin Normal University, Harbin, 150025, PR China.

E-mail addresses: linhuiming@hrbnu.edu.cn (H. Lin), qufengyu@hrbnu.edu.cn (F. Qu).

https://doi.org/10.1016/j.apcatb.2018.11.033
Received 11 September 2018; Received in revised form 1 November 2018; Accepted 13 November 2018
Available online 15 November 2018
0926-3373/ © 2018 Elsevier B.V. All rights reserved.

nanomaterials to reveal the enhanced photocatalysis. Most of them belong to the type-II heterostructure, in which the spatial separation of the electrons and holes would be improved but the redox ability would be greatly reduced. In contrary, the Z-scheme mechanism, the reduced electrons in the lower conduction band (CB) would recombine with the oxidative holes in the lower valance band (VB) between the two semiconductors, causing enhanced separation efficiency as well as the stronger redox ability of the photogenerated charges [26–28]. Especially, in the work of Fu et al., the Z-scheme photocatalysts of $MoSe_2$/graphene/HfS_2 and $MoSe_2$/N-doped graphene/HfS_2 nanocomposites are verified by density functional theory calculations for hydrogen production [24]. Wei et al. have successful synthesized a Z-scheme photocatalyst of Er^{3+}:$YAlO_3$/Ta_2O_5-$CaIn_2S_4$/$MoSe_2$-RGO for visible-light photocatalytic hydrogen evolution [25]. Most of them needed electron mediators to insure the Z-scheme. However, there is not any report to construct direct Z-scheme for $MoSe_2$ based photocatalysts [29–34].

Recently, the synthesis of $MoSe_2$ nanomaterials is mainly derived from the chemical exfoliation, chemical vapor deposition (CVD), solid state reaction and solution chemical method, the low yield and complicated/rigorous operation further limits their development [35–39]. In this work, the uniform hollow $MoSe_2$ nanospheres were synthesized by a facile solvothermal method without any template/surfactant addition. It is the first time to prepare hollow $MoSe_2$ nanomaterial via a one-pot strategy. By varying the reaction time, the formation mechanism was investigated, showing that the novel hollow structure is derived from the Kirkendall Effect. All the nanospheres are assembled by many nanosheets to induce the porous structure of the samples. To construct the heterostructure, $CdCl_2{\cdot}2.5H_2O$ was added as Cd source to obtain hollow $MoSe_2$/CdSe nanospheres about 280 nm in size. The as-synthesized hollow $MoSe_2$/CdSe nanospheres reveal the high photoreduction for Cr(VI) solution (125 mg/g, simulated sunlight), ascribed to the high absorption of full spectrum, porous hollow structure and effective separation of photo-generated electron and hole. The photocatalytic process was further studied in detail to show that the Langmuir single-layer adsorption behavior, low pH value condition, and thermal effect also benefit to the high photoreduction performance. The energy band configuration was further surveyed by VB-XPS and density functional theory (DFT) computation, showing the direct Z-scheme mechanism of $MoSe_2$/CdSe catalysts. The appropriate redox activity also allows the high water splitting ability under simulated sunlight illumination.

2. Result and discussion

Firstly, the hollow $MoSe_2$ nanospheres were synthesized by a facile solvothermal method and the growth process is described in Fig. 1. Under solvothermal treatment for 1 h, the solid nanospheres with smooth surface can be obtained about 400 nm in size. After 6 h, the core-shell nanostructure with 250 nm core can be found from Fig. 1D–F. With the increase of reaction time to 12 h, the core is further dissolved to nearly disappear. M3 reveals the hollow nanospheres assembled by curly nanosheets. Further prolonging the reaction over 36 h, these $MoSe_2$ nanosheets go on growth, inducing the shell of hollow spheres increase from 40 (M3) to 80 nm (M4). In view of other reports, the formation of hollow structure can be ascribed to the Kirkendall Effect [40,41]. HRTEM image (Fig. 1M) further reveals the layer structure of these nanosheets and the lattice fringes of $d_{002} = 0.66$ and $d_{103} = 0.24$ nm confirms the 2H-$MoSe_2$ (JCPDS card, no. 29-0914) crystal structure. Moreover, the interlayer spacing d_{002} is slightly larger than that of the $MoSe_2$ bulk (0.64 nm), suggesting the several layers of the every $MoSe_2$ nanosheet. This result is in agreement with XRD (Fig. 1N). With increase of reaction time, the crystallinities of corresponding samples are gradually enhanced. Compared with the common methods, the solvothermal method used in this paper also reveals rather high yield about 87.5% (inset of Fig. 1M). Elemental compositions and valence states of the as-prepared samples were further investigated by XPS. As shown in Fig. S1B, the peaks at 228.7 and 231.8 eV are attributed to Mo $3d_{5/2}$ and $3d_{3/2}$ spin orbital that demonstrates its +4 state rather than +6 state of Mo, confirming the MoO_4^{2-} has been fully reduced to Mo^{4+} of $MoSe_2$. In addition, the peak of $3d_{5/2}$ can be further divided into 228.6 eV and 229.8 eV while the peak of Mo $3d_{3/2}$ is also divided into 231.6 eV and 232.8 eV. The divided peaks at 229.8 eV and 232.8 eV are attributed to Mo $3d_{5/2}$ and $3d_{3/2}$ of the 2H polymorph, respectively. Meanwhile, the peaks of Mo $3d_{5/2}$ and $3d_{3/2}$ at 228.6 eV and 231.6 eV exhibit a part of the 1T phase [42–44]. Similarly, the characteristic peak of Se 3d locate at 55.1 eV was also shown in Fig. S1C, which belonging to the $3d_{3/2}$ for the −2 state of Se, and it can also be divided into two peaks of $3d_{5/2}$ (54.7 eV) and $3d_{3/2}$ (55.5 eV), which are ascribed to 1T and 2H phase, respectively. Besides, the HTREM image also testifies (Fig. S2) the 1T (hexagonal) and 2H phase (honeycomb) of the as-synthesized $MoSe_2$. The porous structures of the four samples are determined by N_2 adsorption/desorption. From Fig. S3A, all of them show type IV isotherms with H3 hysteresis loop, illustrating the accumulational porous structure of the samples. With the hollow structure and thin shell, M3 possess the highest surface area ($26.83\ m^2\ g^{-1}$) and pore volume ($0.103\ cm^3\ g^{-1}$) of all (Table S1). Considering the abundant porous structure, the electrochemical measurements were carried out using hollow $MoSe_2$ nanosphere (M3) as the electrode, showing the high specific capacitance ($350\ F\ g^{-1}$ at $1\ A\ g^{-1}$, $237\ F\ g^{-1}$ at $20\ A\ g^{-1}$) and excellent cycle capability (94% after 5000 cycles, Fig. S4).

In addition, the hollow $MoSe_2$/CdSe heterostructure was also prepared by the same method of M3, just by putting in $CdCl_2{\cdot}2.5H_2O$ as Cd source. The SEM images of samples MC1, MC2 and MC3 are shown in Fig. S6A–C, it is still present a uniform spherical shape for $MoSe_2$/CdSe heterostructures and the TEM images reveal the structure of $MoSe_2$/CdSe heterostructures also remains the hollow structure with 280 nm in size (Fig. 2A and B), which is smaller than that of pure $MoSe_2$ (M3, 400 nm). Moreover, the increase of $CdCl_2{\cdot}2.5H_2O$ induces the decrease of the shell thickness of MC2. Further increasing the Cd source, MC3 exhibits partial collapse hollow structure (Fig. 2C). All the hollow nanospheres are assembled by many small nanostructures to induce a mass of porous structures as well as high surface areas. As displayed in Table S2, all samples show large surface area about 21.86, 28.62 and $18.46\ m^2\ g^{-1}$ for MC1, MC2 and MC3, respectively (Fig. S7). The largest surface area of MC2 is due to its uniform hollow structure with the thin shell. The high-angle annular dark field (HAADF) image and the corresponding energy dispersive X-ray (EDX) mapping images (Fig. 2D) reveal the uniform elemental distribution of Se, Mo and Cd in the $MoSe_2$/CdSe heterostructure. The crystallographic structure of the as-prepared $MoSe_2$/CdSe heterostructure was tested by XRD in Fig. 2E. All the diffraction peaks well match with the 2H-$MoSe_2$ (JCPDS no. 29-0914) and CdSe (JCPDS no. 77-0021), and no additional impurity phases can be detected. With the most amount of Cd source, MC3 reveals the strongest characteristic peaks of CdSe. The HRTEM image (Fig. 2F) shows the inter-planar spacing of 0.66 and 0.35 nm, attributing to (002) plane of 2H-$MoSe_2$ and (002) plane of CdSe, respectively. The selected area electron diffraction pattern exhibits clear diffraction rings, indicating a high crystallinity of $MoSe_2$/CdSe. And the new emerging diffraction ring (solid line) in Fig. 2H also belongs to (100) plane of CdSe. XPS spectrum of $MoSe_2$/CdSe heterostructure is shown in Fig. 3. Compared with pure $MoSe_2$, the additional characteristic peaks at 405.3 and 412.0 eV are ascribed to Cd $3d_{5/2}$ and $3d_{3/2}$ spin orbital [45]. In view of the above investigation, $MoSe_2$/CdSe heterostructure was prepared successfully.

The photocatalytic reduction of Cr(VI) by these as-synthesized samples was evaluated in Fig. 4. First, the dark reaction for 30 min was carried out to insure the adsorption equilibrium, showing 34.0, 29.0, 37.0, 27.0 and 26.0% adsorption amount (Cr(VI)) for M3, MC1, MC2, MC3 and CdSe, respectively (Fig. 4A). The highest adsorption amount of MC2 is ascribed to the highest surface area of all (Tables S1 and S2).

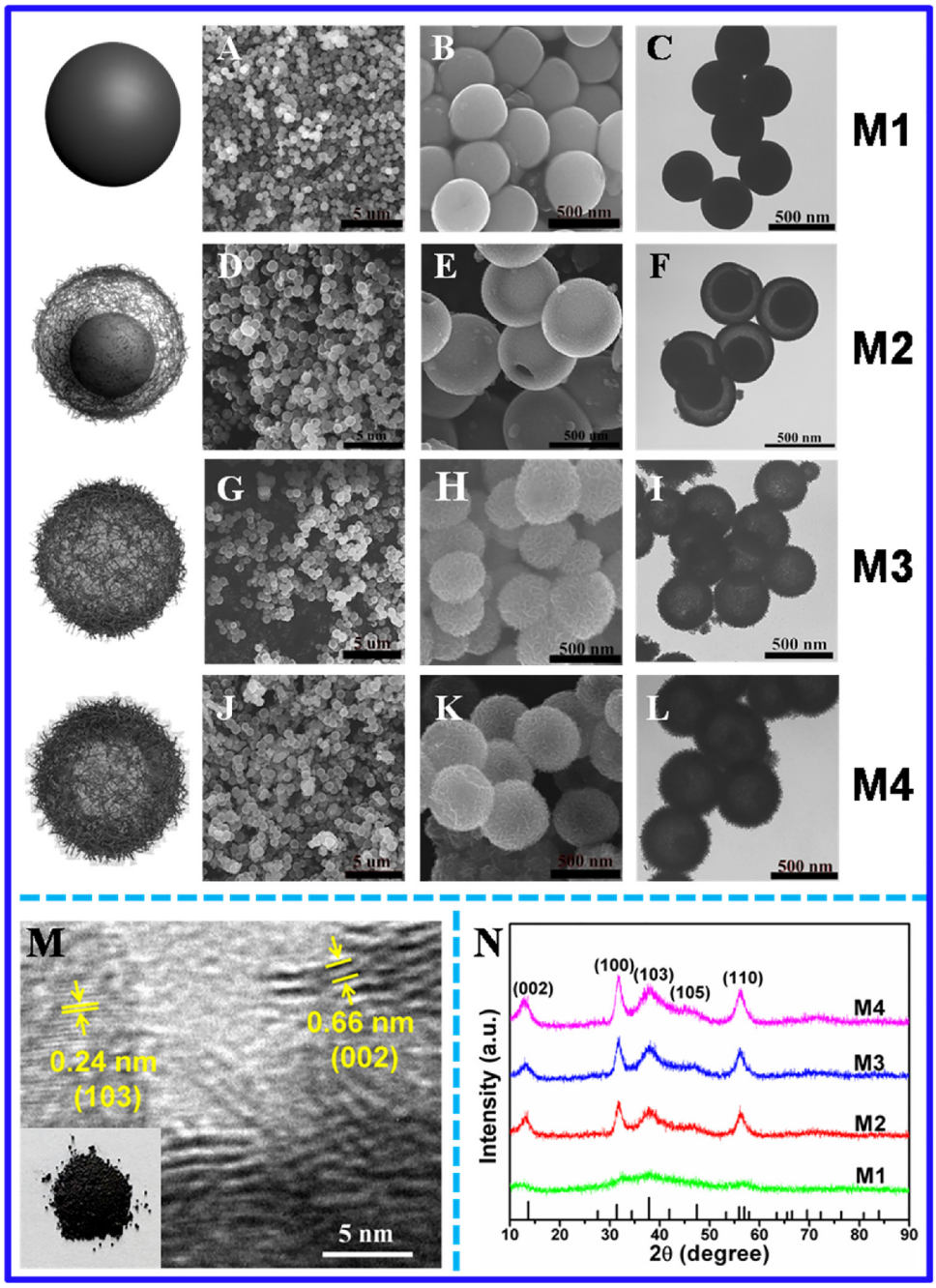

Fig. 1. SEM (A, B, D, E, G, H, J and K) and TEM (C, F, I and L) images of $MoSe_2$ nanospheres with different reaction times (M1: 1 h; M2: 6 h; M3: 12 h; M4: 36 h) at 180 °C. (M) HRTEM image of M3 (inset is the digital picture of $MoSe_2$ production from one pot reaction). (N) XRD pattern of them.

When illumination (Xe lamp used as stimulated sunlight) is introduced, the fast degradation of Cr(VI) can be found from $MoSe_2$/CdSe composites. After 80 min illumination, the degradation rate can reach 81.0, 98.3 and 70.0% for MC1, MC2, and MC3. However, the degradation rate of M3 (pure $MoSe_2$) and CdSe is just 53.0 and 55.0%. The higher photoreduction behaviors of MCs benefit from the effective charge separation in $MoSe_2$/CdSe heterostructure.

Furthermore, the photocatalytic degradation kinetics were researched to further demonstrate the reduction of Cr(VI). The typical Langmuir–Hinshelwood (L–H) model was used to analyze these data. The corresponding formula is shown in following:

$$r = -\frac{dC}{dt} = \frac{k'KC}{1} + KC \quad (1)$$

where r is the rate of Cr(VI) reduction, k' is the rate constant, C is the Cr (VI) concentration, and K is the adsorption coefficient. In brief, formula (1) can be converted to the formula (2):

$$\ln(C/C_0) = -kt \quad (2)$$

where C_0 is the initial concentration of the Cr(VI) and k is rate constant. The rate constant k can be calculated by the slope of the fitting curves of $\ln(C/C_0)$ versus time (t) as exhibited in Fig. 4B. All samples reveal the good linear relationship between $\ln(C/C_0)$ and irradiation time t, implying that these degradation performances belong to the Langmuir–-Hinshelwood model. It can be seen that MC2 displays the highest rate constant (0.0441 min^{-1}) followed with MC1 (0.0167 min^{-1}), MC3 (0.0110 min^{-1}), CdSe (0.0060 min^{-1}) and M3 (0.0045 min^{-1}). The stability of photocatalyst is significant for the practical application, so the cycling test of photocatalytic activity was measured under

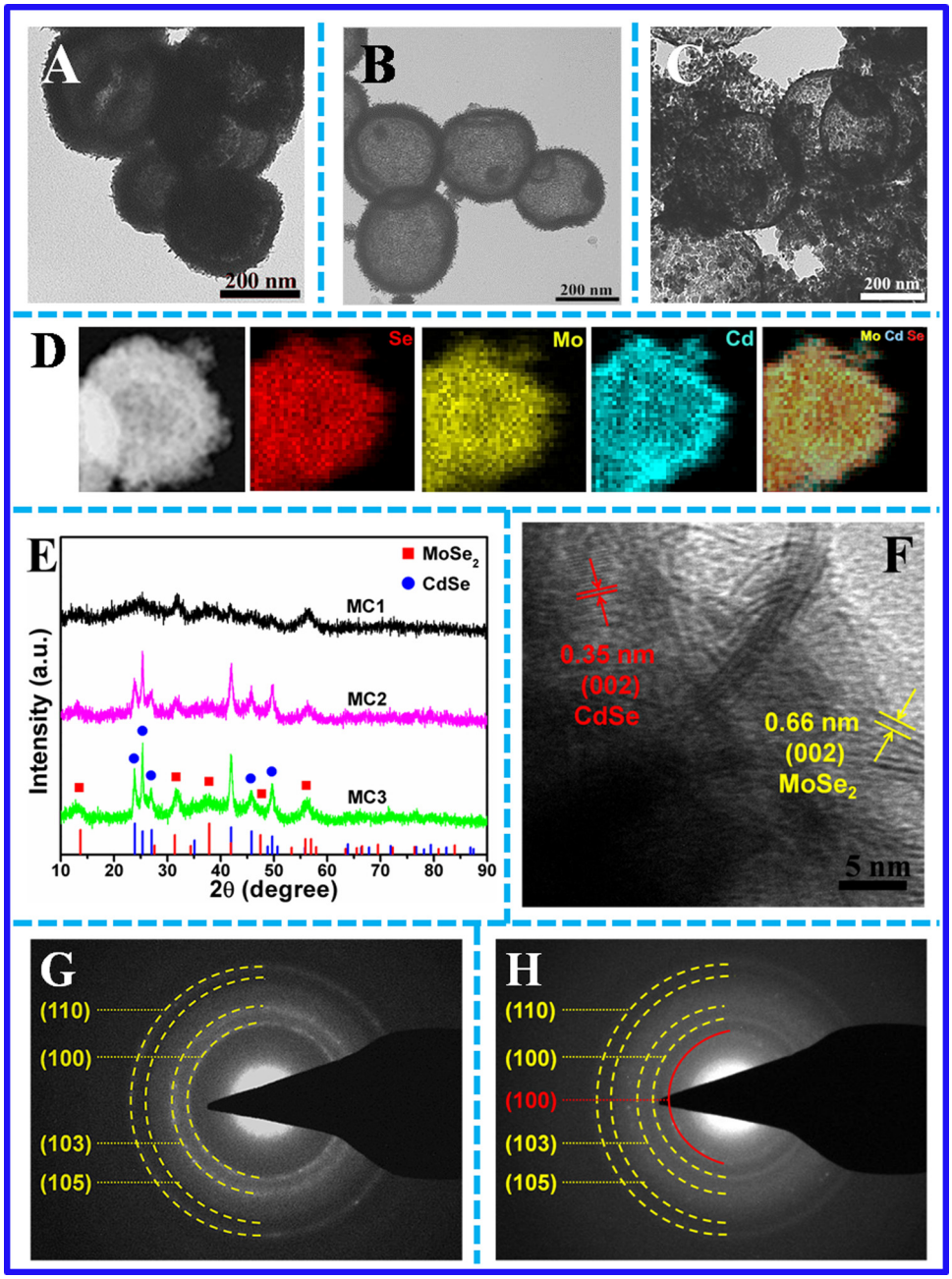

Fig. 2. TEM images of (A) MC1 (CdSe: 7 wt.%). (B) MC2 (CdSe: 18.5 wt.%). (C) MC3 (CdSe: 27.5 wt.%). (D) HAADF-STEM image of MC2 and the corresponding STEM-EDX elemental mapping images for Se, Mo and Cd. (E) XRD of MC1, MC2 and MC3. (F) HRTEM image of MC2. SAED pattern of pure $MoSe_2$ (G) and $MoSe_2$/CdSe (H) nanocomposite.

irradiation for five times (Fig. 4C). After cycling five times, MC2 also remains 90.1% reduction rate exhibiting the excellent photo-stability, and the inappreciable decrease for photocatalytic activity is because of the loss of material in collection process.

In addition, to further investigate the utilization of light, the reductions of Cr(VI) by MC2 under UV, visible and NIR light were carried out by use Xe lamp as light source with cutoff filters ($\lambda < 400$ nm, 780 nm $> \lambda >$ 400 nm, $\lambda >$ 800 nm). As shown in Fig. 4D, it takes 80 min for MC2 to reveal 89.6% and 79.0% reduction under visible and UV irradiation. More importantly, MC2 also reveals the comparative photocatalytic activity (82.2%) under NIR irradiation. The efficient utilization of the full spectrum light makes potential application of the as-synthesized on solar potocatalysis.

Beside the light utilization and charge transportation/separation, the adsorption capacity of Cr(VI) onto the surface of catalyst is also another dominant factor in the photocatalysis. To further observe the adsorption and photo-reduction activity of MC2, the photocatalytic performance was investigated by varying the concentration of Cr(VI) solutions (50–150 mg L^{-1}). From Fig. 5A–E, all the UV–vis absorption spectra of Cr(VI) show that the absorption peaks decrease with the irradiation time going on, and the percent of Cr(VI) reduction can reach 100.0% (50 mg L^{-1}, 40 min), 99.5% (75 mg L^{-1}, 60 min), 98.3% (100 mg L^{-1}, 80 min), 93.0% (125 mg L^{-1}, 140 min) and 83.3% (150 mg L^{-1}, 160 min), respectively. In view of the above data, the equilibrium adsorption isotherm (dark condition) of MC2 to Cr(VI) solution can be calculated as displayed in Fig. 5F. With the increase of the Cr(VI) concentration, the adsorption amount of Cr(VI) also increases gradually until the adsorption amount reaches the saturation amount (40 mg g^{-1}). The adsorption isotherm is assigned to a type I curve, characteristic Langmuir isotherm. Then the measured

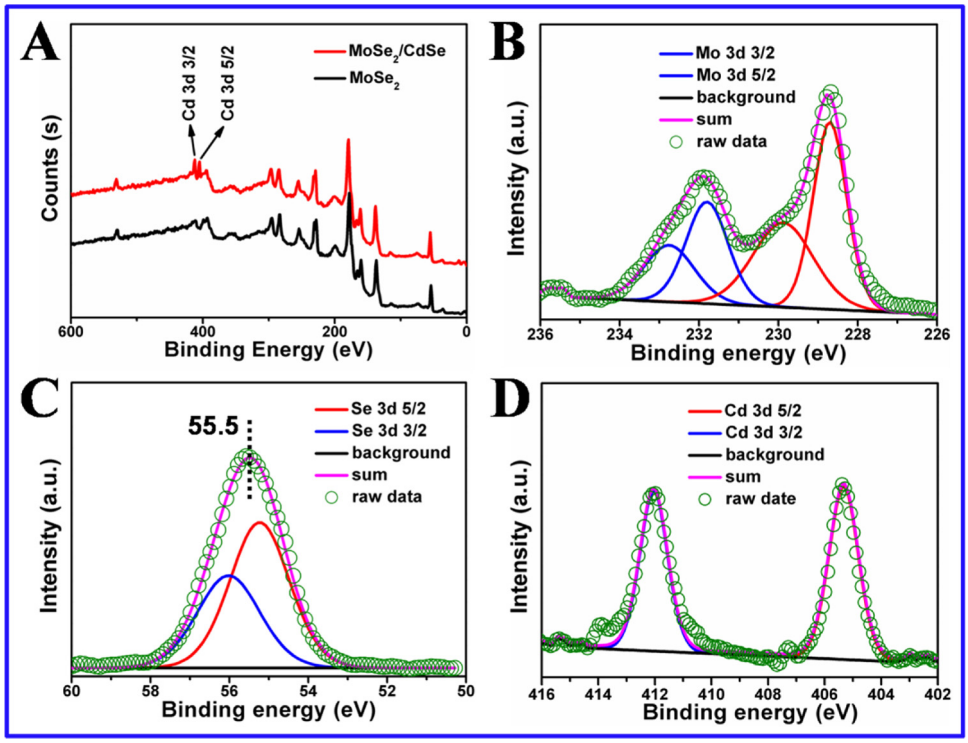

Fig. 3. (A) XPS survey scan of $MoSe_2$/CdSe and $MoSe_2$ nanocomposite. High-resolution XPS spectra of the (B) Mo 3d, (C) Se 3d and (D) Cd 3d regions of $MoSe_2$/CdSe.

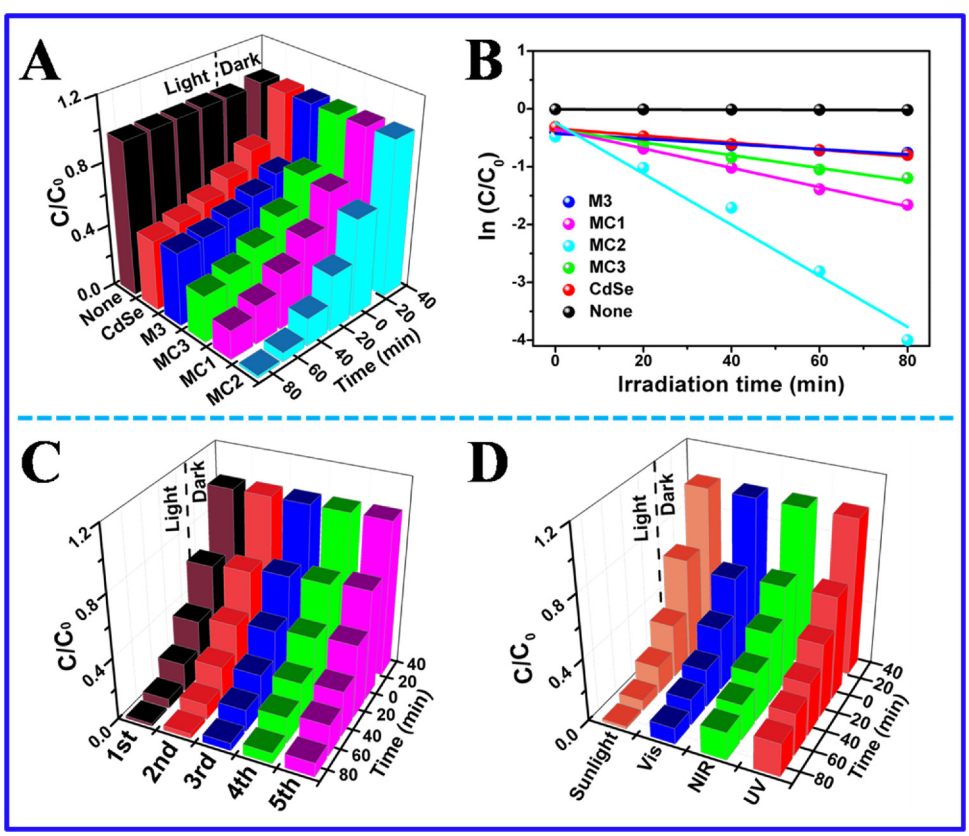

Fig. 4. (A) Photocatalytic degradation rates of Cr(VI) with the five samples and without sample. (B) Photocatalytic reaction kinetics of Cr(VI) with reaction time. (C) Cycling tests of the photocatalytic activity of MC2. (D) Photocatalytic degradation rates of Cr(VI) for the sample MC2 under differernt lights.

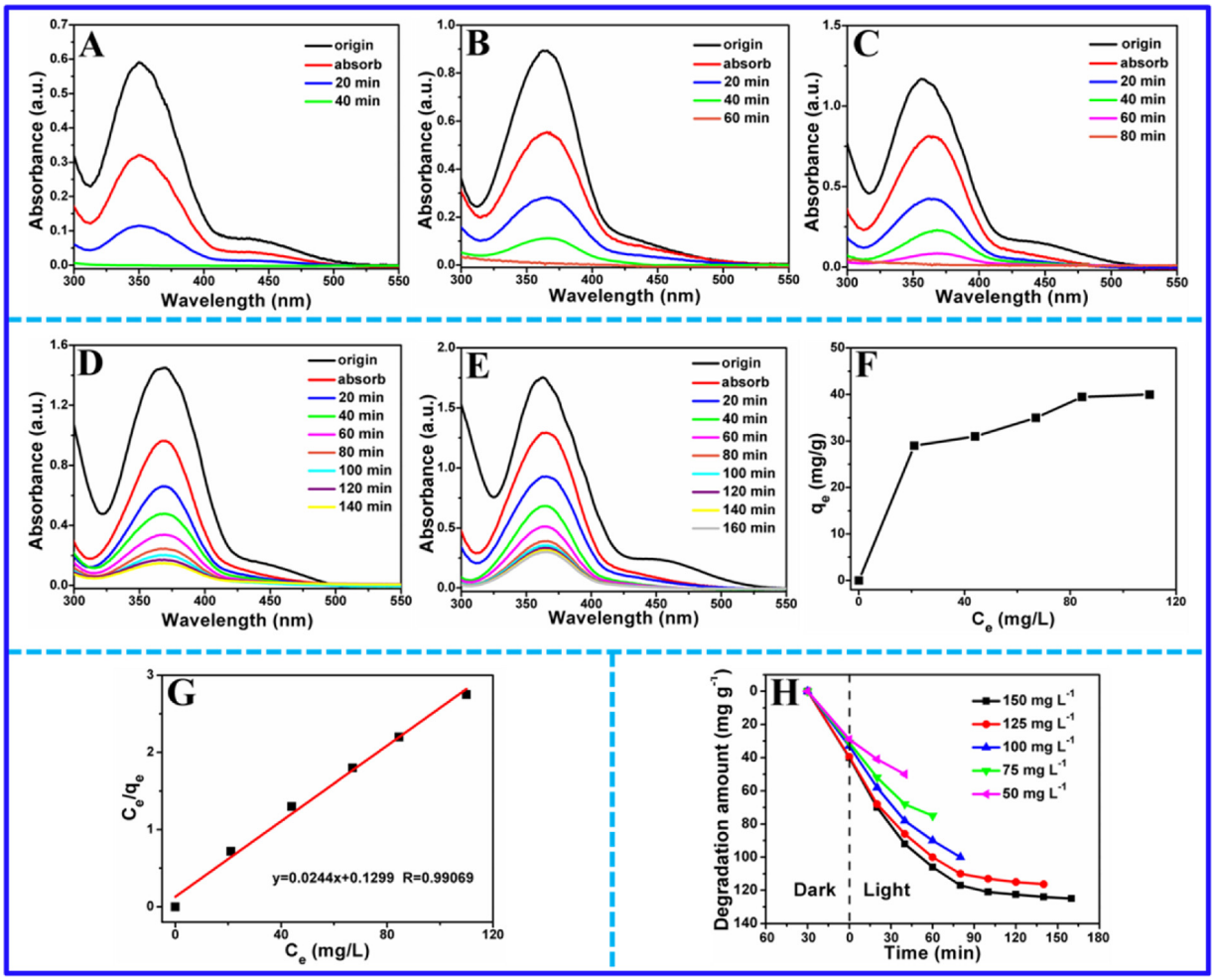

Fig. 5. UV–vis spectra of Cr(VI) solution under sunlight in the presence of sample MC2, (A) 50 μg mL^{-1}, (B) 75 μg mL^{-1}, (C) 100 μg mL^{-1}, (D) 125 μg mL^{-1} and (E) 150 μg mL^{-1}. (F) The curve of the degradation ability of MC2 heterostructure to the variated concentrations of Cr(VI) in degradation systems and the corresponding linear Langmuir transform of the curve (G). (H) Variation of the degradation capability of the MC2 ($K_2Cr_2O_7$/catalyst, mg/g) to degradation time.

equilibrium adsorption of Cr(VI) on the photocatalyst was further analyzed by fitting the equilibrium adsorption data by Langmuir equation:

$$\frac{c_e}{q_e} = \frac{1}{q_m k} + \frac{c_e}{q_m} \tag{3}$$

Where c_e is equilibrium concentration, q_e is the equilibrium adsorption amount (mg g^{-1}), k is the Langmuir constant and q_m is the theoretical maximum monolayer adsorption amount (mg g^{-1}). The corresponding linear Langmuir transform of the isotherm is shown in Fig. 5G, and all the adsorption data fit linear Langmuir relationship very well with the theoretical maximum adsorption value (q_m = 40.9 mg g^{-1}) closed to the measured values (40.0 mg g^{-1}). It is known that the Langmuir adsorption belongs to typical monolayer adsorption, making the favorable contact between catalyst and Cr(VI). The high adsorption capacity and Langmuir adsorption behavior benefits the photocatalytic capacity of MC2 to reduce Cr(VI). Moreover, the photocatalytic capability is further evaluated using $K_2Cr_2O_7$/catalyst (mg g^{-1}) that is recorded to different irradiation times as shown in Fig. 5H. MC2 reveals 50 mg g^{-1} photoreduction capability for 50 mg L^{-1} of Cr(VI) solution under irradiation for 40 min. With the increase of Cr(VI) concentration to 150 mg L^{-1}, the capability also increases to 92 mg g^{-1} (40 min) and that can reach up to 125 mg g^{-1} after 160 min.

Besides, the influence of pH value on photocatalysis performance was also studied by varying pH value (2.0–7.0). From Fig. 6A, the Cr (VI) reduction is enhanced by decreasing the pH value [46]. And the photoreduction capacity can increase from 126.6 mg g^{-1} (pH = 7.0) to 194.0 mg g^{-1} (pH = 2.0). As we know, at low pH condition, Cr(VI) is mainly present as $Cr_2O_7^{2-}$ with the potential of $E(Cr_2O_7^{2-}/Cr^{3+})$ about 1.23 eV. However under neutral or even basic condition, it is CrO_4^{2-} as the major Cr(VI) species with the potential of $E(CrO_4^{2-}/Cr(OH)_3)$ about −0.13 eV. The increased photoreduction activity along with the decrease of pH value is ascribed to the high $E(Cr_2O_7^{2-}/Cr^{3+})$, making it is reduced easily. Notably, the increased adsorbing capacity of MC2 as the decrease of pH value can be ascribed to the weaken electrostatic repulsion between MC2 (zeta potentials in Fig. S8) and Cr(VI) species (CrO_4^{2-} or $Cr_2O_7^{2-}$). Moreover, under neutral or even basic condition, the $Cr(OH)_3$ precipitate as the reduction product coated outside the catalyst to limit the catalytic performance. Considering the excellent catalysis behavior in acid condition, the photoreduction capability of MC2 to Cr(VI) at pH = 3 was further investigated. As exhibited in Fig. 6B, go on elevating the Cr(VI) concentration, the photoreduction capability of MC2 increases obviously. After 60 min illumination, photoreduction capability can reach 206.8 mg g^{-1} for 250 mg L^{-1} Cr (VI) solution (82.7%).

It is known that, $MoSe_2$ is a typical photothermal agent as it can absorb light energy to convert it to heat, and it is widely used on photothermal therapy for anticancer [47–49]. Here, the influence of photothermal on catalysis was also surveyed. The temperatures during photodegradation process with (condition-3) or without (condition-2) circulating water bath were tested and recorded by an infrared imaging device every 20 min. As displayed in Fig. 6C, the condition-3 remains

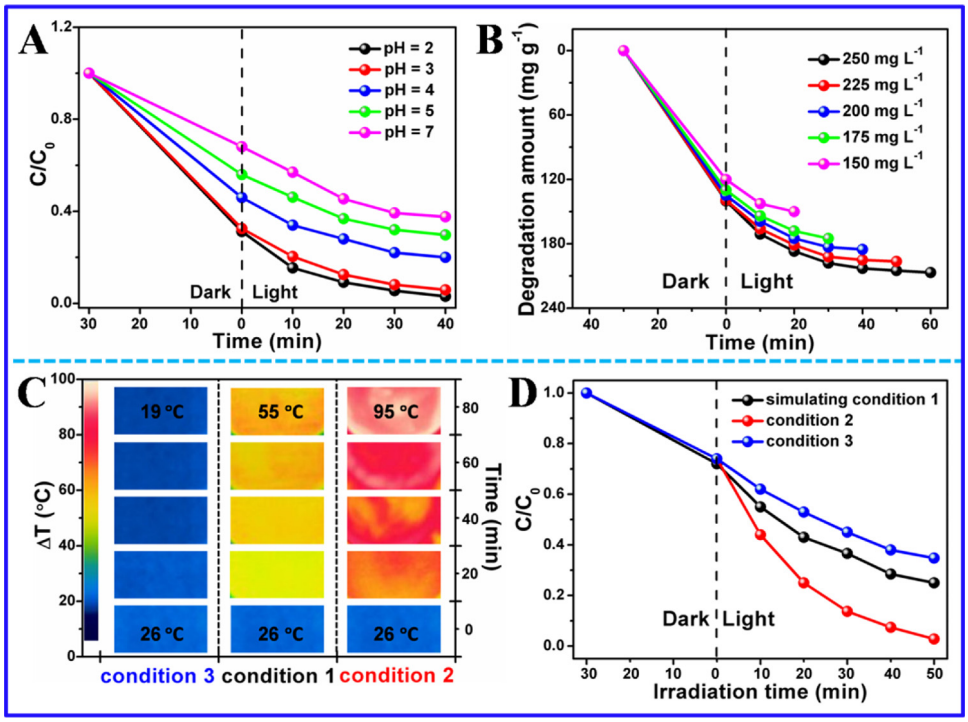

Fig. 6. (A) Photocatalytic degradation rates of Cr(VI) for the sample MC2 under different pH ($C(K_2Cr_2O_7)$ = 200 μg mL^{-1}). (B) Variation of the degradation capability of MC2 ($K_2Cr_2O_7$/catalyst, mg/g) to degradation time (pH = 3). (C) Heating images of dispersions under simulated sunlight irradiation. (condition 1: pure water without circulating cooling; condition 2: the dispersion of 1 mg mL^{-1} of MC2 without circulating cooling; condition 3: 1 mg mL^{-1} of MC2 dispersion with circulating cooling at 19 °C). (D) Cr(VI) photocatalytic degradation rates of MC2 (1 mg mL^{-1}) under circulating cooling at 55 (condition 1), 19 °C (condition 3) and without any circulating cooling (condition 2).

the low circulating water bath temperature of catalytic system 26–19 °C after photocatalysis for 80 min. However, without circulating water bath, the catalyst suspension exhibits the fast temperature rise from 26 to 95 °C owing to the photothermal effect of $MoSe_2$ (condition-2, Fig. 6C). Furthermore, considering the pure water can also absorb the light to enhance the temperature, the temperature of pure water without circulating water bath was also detected, elevating from 26 to 55 °C (condition-1, Fig. 6C). From Fig. 6D, the photothermal effect induces the fast photoreduction capacity to 97% within 50 min (condition-2). To further confirm the photothermal-enhanced catalysis, the photocatalysis was carried out in 55 °C (water bath) to detect the influence of thermal effect from water. Under the condition, the photoreduction just reaches 75%. However, that is just 65% under circulating water bath (condition-3 in Fig. 6C). It is believed that, the thermal effect is in favour of charge transfer that benefits the photocatalysis [50–52]. Based on Figs. 6C, D and S9, the photothermal effect of $MoSe_2$ makes the thermal-enhanced catalysis behavior.

Light harvest, charge transportation and separation are crucial to determine the final photocatalysis behavior. Fig. 7A shows the UV–vis diff ;uses absorption spectra of M3, MC1, MC2, MC3 and CdSe. The pure $MoSe_2$ (M3) exhibits strong absorption in the full spectrum region, and its absorption edge of M3 is about 810 nm (1.53 eV, Fig. S11A). In addition, pure CdSe nanoparticle was also synthesized using the same method as $MoSe_2$/CdSe without Mo source input (Fig. S10). And its absorption edge and band gap energy is inferred to be 734 nm and 1.69 eV, so that the combination of most amount of CdSe, MC3 (CdSe: 27.5 wt%) shows the lowest absorption beyond 800 nm (Fig. 7A). With good harvest of the broad spectrum light, the as-synthesized samples exhibit the excellent photocatalysis behavior with eff ;ective utilization of solar energy (Fig. 4D). In addition, the advantageous hollow structure of $MoSe_2$/CdSe heterostructure which assembled with layered nanosheets insures the multi-reflection and multi-utilization of light (Fig. S12). The valance bands (VB) of the samples were determined by VB XPS spectra as shown in Fig. 7B and C. It can be seen that the VB value of M3 and CdSe is 0.24 and 1.22 eV (vs. Fermi level), respectively. Here, DFT calculations (Fig. 7D and E) were performed to speculate the work function of $MoSe_2$ (4.626 eV) and CdSe (4.710 eV), accordingly their E_f is calculated to be 0.126 and 0.210 eV (vs. NHE). Moreover, open circuit potential (OCP) technique was also measured to reveal E_f of $MoSe_2$ (0.061 eV) and CdSe (0.123 eV) that is agreed with DFT (Fig. S7C and D) [53–55]. Based on the above investigation, the VB and CB value of $MoSe_2$ and CdSe can be confirmed equal to 0.366 and −1.164 eV and 1.430 and −0.260 eV, respectively.

It is known that the energy band configuration of a semiconductor heterostructure is significant to determine the spatial dynamics behavior of the photoinduced electrons-holes across the heterointerface [54,56–60]. When the $MoSe_2$/CdSe heterostructure is constructed, the electron can transfer between the interfacial of $MoSe_2$ and CdSe to balance the Fermi level of them. The above-mentioned experimental and DFT computation results indicate that the E_f position of $MoSe_2$ is more negative than that of CdSe, so that the accumulated electrons on the E_f of $MoSe_2$ would flow to the CdSe across the heterointerface, which results in a positive shift of E_f in $MoSe_2$ and a negative shift of E_f in CdSe (Fig. 8A). Likewise, the shifted E_f in the $MoSe_2$/CdSe heterostructure could also cause the negative energy band bending of $MoSe_2$ and the positive energy band bending of CdSe. In this way, the CB position of CdSe is closer to the VB position of $MoSe_2$ at the heterointerface. Illuminated by high-energy light, such as UV and visible light, both $MoSe_2$ and CdSe can be excited, the electrons could be excited to the CB with simultaneous generation of the same amount of holes in the VB. From the energy band structure diagram of $MoSe_2$/CdSe in Fig. 8B, it could be found that due to the band bending and the formed interface electric field induces the photogenerated electrons on the CB of CdSe spatially transfer to VB of $MoSe_2$ to make sure the Z-Scheme mechanism, leaving the photoinduced electron in the CB of $MoSe_2$ and the photogenerated hole in the VB of CdSe. Furthermore, according to previous reports [61], the changes of electronic density on the different surfaces of a heterostructure was demonstrated by the change of binding energies in XPS spectrum. Therefore, the XPS characterization of $MoSe_2$, CdSe and their composite was carried out as shown in Fig. S13. Compared with the XPS spectra of M3 (Fig. S13A), Mo 3d state of MC2 (Fig. S13B) moves to the direction of lowerenergy, revealing the higher of electron density of MC2. Meanwhile, the Cd 3d state of MC2 (Fig. S13D) shifts to higherenergy region (low electron density) in comparison with that of M3 (Fig. S13C). Illusrating the electrons were migrated from CdSe to $MoSe_2$ for the $MoSe_2$/CdSe nanocomposite.

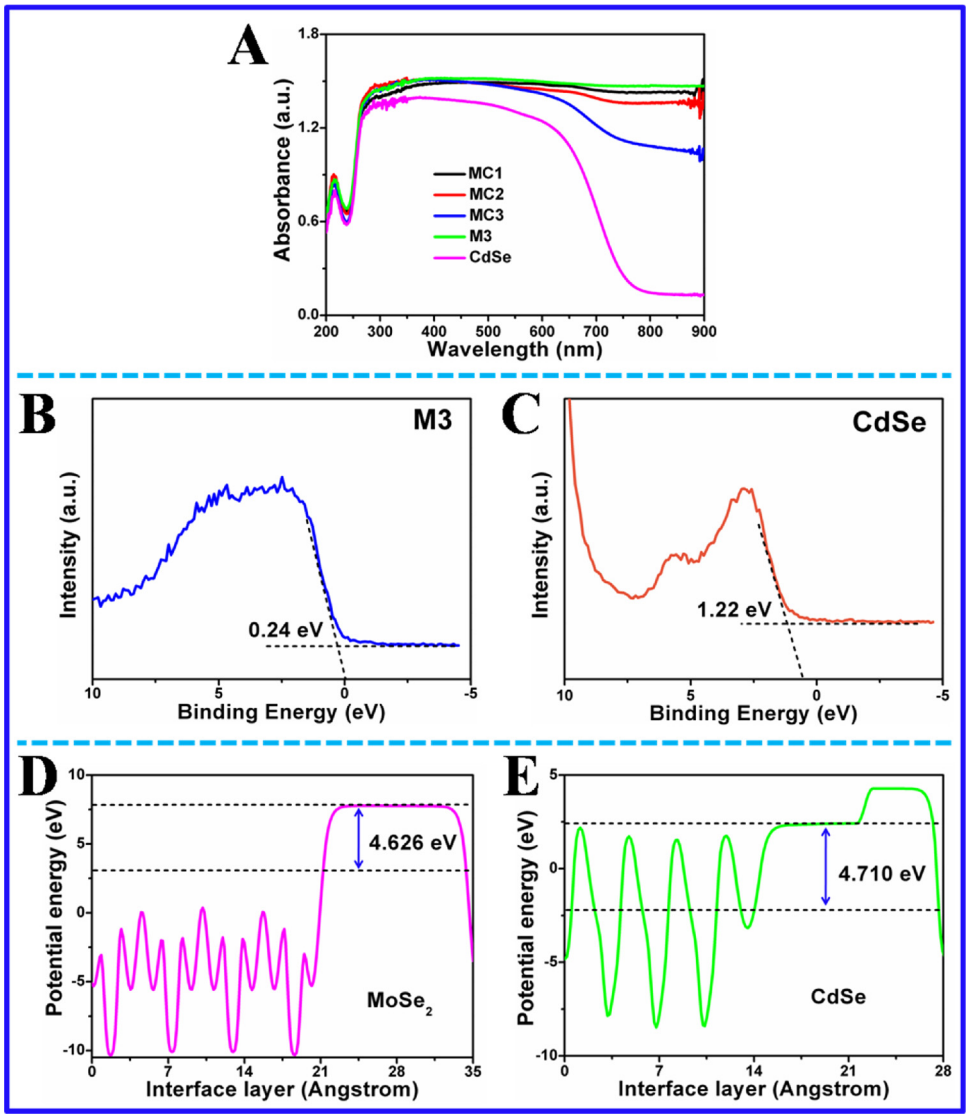

Fig. 7. (A) Absorption edges of the sample M3, MC2 and pure CdSe nanoparticles. Valence-band XPS spectrum of M3 (B) and pure CdSe (C). (D, E) DFT calculated potential diagrams of $MoSe_2$ and CdSe surfaces in vacuum.

Based on above study, this migration pathway of the photogenerated electrons is identified with a direct Z-scheme photocatalyst [62–68]. However, under NIR light (> 800 nm) irradiation, only $MoSe_2$ could be excited so that there is not Z-scheme (Fig. 8C). In any case, the electron in CB (−1.164 eV) is more negative than Cr(VI)/Cr(III) (+0.51 eV) even under NIR condition, therefore MCs are the novel photocatalysts to reduce Cr(VI) [69].

The charge transfer efficiency at the interface of photocatalyst/electrolyte was analyzed according to the EIS. The smaller radius of the arc suggests that a faster interfacial charge migration and more effective separation of charge carriers [10,11]. From Fig. 8D, MCs exhibit the smaller arc of semicircle than that of pure $MoSe_2$ (M3), implying the more efficient charge transfer and recombination inhibition of the heterostructure. Among $MoSe_2$/CdSe, MC2 exhibits the smallest arc of semicircle suggesting the best interfacial charge transfer as well as the best photocatalytic capacity compared with other samples (Fig. 4). In addition, the transient photocurrent responses under stimulated sunlight are shown in Fig. 8E, it can be observed that the photocurrent is increased rapidly with the light is switched on, illustrating the photo-induced electron and hole. And that also quickly drops to zero when light is removed owing to the recombination of electron and hole. The highest photocurrent also demonstrates the fastest photocatalytic behavior of MC2. Fig. 8F shows the photoluminescence (PL) of them. It can be found that the intensity of MC2 is much weaker than other samples. Furthermore, the average lifetimes of charge carriers are calculated to be 1.32, 1.42 and 1.75 μs for CdSe, M3 and MC2 through their transient PL spectra (Fig. S14), which further confirms that the recombination of photo-induced electrons and holes in MC2 can be eff ;ectively inhibited. Besides, the photocurrent of MC2 was also further measured under UV, visible and NIR light as shown in Fig. 8G. It can be observed that the photocurrent under visible light is highest followed with NIR and UV light, which matches well with the photocatalytic activity of MC2 (Vis > NIR > UV, Fig. 4). Although the UV light with high energy can induce the electron and hole separation of $MoSe_2$ and CdSe, the low proportion (below 10%) in full spectrum results in the low photocurrent as well as low photocatalytic performance on UV light. With closed proportion in full spectrum of visible light, the lower photocurrent and photocatalysis behavior of NIR light is ascribed to the lower utilization, because CdSe cannot absorb and utilize NIR light (> 800 nm). Based on the above investigation, the great harvest of light, eff ;ective separation of photo-induced electrons and holes, and large surface make MC2 as a potential full spectrum photocatalyst to reduction of Cr(VI). Compared with the previous reports, MC2 also exhibits the excellent photocatalysis capacity (Table S3).

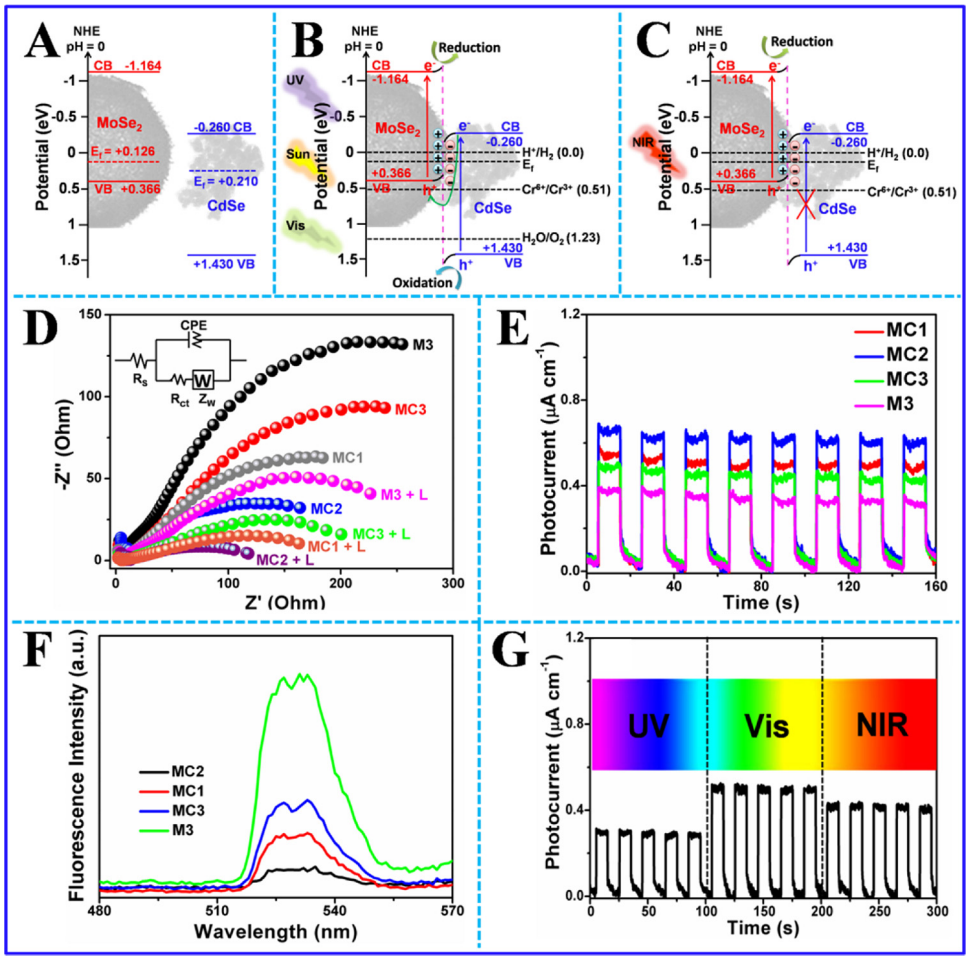

Fig. 8. (A)–(C) The photocatalytic mechanism of $MoSe_2$/CdSe heterostructure with different lights irradiation. (D) Nyquist polt of the four samples before and after sunlight irradiation. (E) Transient photocurrent responses of M3, MC1, MC2 and MC3 under the simulative sunlight. (F) Fluorescence spectra of the four samples. (G) Transient photocurrent responses of MC2 under UV–vis-NIR lights.

Based on the above investigation, the Z-Scheme mechanism in $MoSe_2$/CdSe heterostructure makes sure the high redox capacity of MC2. From Fig. 8B, the electron in CB level of $MoSe_2$ (−1.164 eV) is also more negative than the H^+/H_2 (0.0 eV), and the hole in VB level of CdSe (1.430 eV) is more positive than the H_2O/O_2 potential (+1.230 eV) so that $MoSe_2$/CdSe heterostructure would be considered as potential photocatalyst for water splitting [23,34,42,70–73]. Firstly, H_2 production were recorded in the presence of Na_2S and Na_2SO_3 as the sacrificial agents as shown in Fig. 9A–C. Under Vis-light illumination, the amount of H_2 increases with prolonging the irradiation time and reaches 16.38 mmol g^{-1} after 2.5 h, indicating MC2 can serve as an efficient photocatalyst for H_2 evolution without any other cocatalysts such as Pt. The low amount of H_2 production (5.06 mmol g^{-1}) from M3 is attributed to the fast recombination of photogenerated charges in pure $MoSe_2$. The photocatalytic stability of MC2 was carried out by repeating the experiment five times as displayed in Fig. 9B. Continuous H_2 evolution was detected with no obvious attenuation in these recycles, indicating that MC2 acts as a stable photocatalyst for H_2 evolution (Fig. S15). The slight decrease of the H_2 production during the recycling experiments is owing to the loss of catalysts during the collection process. Moreover, the photocatalytic performances acted by different lights were also surveyed, showing 4.96 (UV), 5.98 (NIR), 6.55 (VIS) and 7.12 (full spectrum) mmol h^{-1} g^{-1} H_2 evolution (Fig. 9C). In addition, the O_2 evolution was also investigated with Cr(VI) as the sacrificial agent. From Fig. 9D, the O_2 evolution also increases with irradiation and it reaches 0.87 mmol g^{-1} after 2.5 h. While, the trace amount of O_2 was detected from M3, implying the hole in VB of M3 cannot oxide H_2O to form O_2. The O_2 production by using MC2 as photocatalyst further confirms the novel Z-Scheme mechanism in $MoSe_2$/CdSe heterostructure, which insure the high redox capacity of MC2, so that MC2 can be considered as potential photocatalyst for water splitting [74–77]. To evaluate the availability of light for the catalyst, the wavelength dependent apparent quantum yield (AQY, Fig. 9E) of MC2 for H_2 evolution was calculated as the formula (4).

$$AQY = \frac{N_e}{N_p} \times 100\% = \frac{2 \times M \times N_A \times h \times c}{S \times P \times t \times \lambda} \times 100\% \quad (4)$$

where N_e is the amount of reaction electrons, N_p is the incident photons, N_A is Avogadro constant, M is the amount of H_2 molecules, c is the speed of light, h is the Planck constant, P is the intensity of the irradiation, S is the irradiation area, t is the photoreaction time and λ is the wavelength of the monochromatic light [69,78]. Ultimately, the sample MC2 exhibits a comparatively high AQY of 27.2% under the incident monochromatic light of 670 nm, which indicating the as-prepared catalyst has a high H_2 evolution capacity (Tables S4 and S5) [28,62–68].

3. Conclusions

In summary, for the first time the hollow $MoSe_2$ nanospheres (400 nm) were prepared by one-pot solvothermal method without any surfactant/template assistance. By varying reaction time, these products undergo solid, core-shell, and hollow change, and the formation mechanism could be ascribed to the Kirkendall Effect. Moreover, just by adding $CdCl_2 \cdot 2.5H_2O$ as Cd source, the hollow $MoSe_2$/CdSe

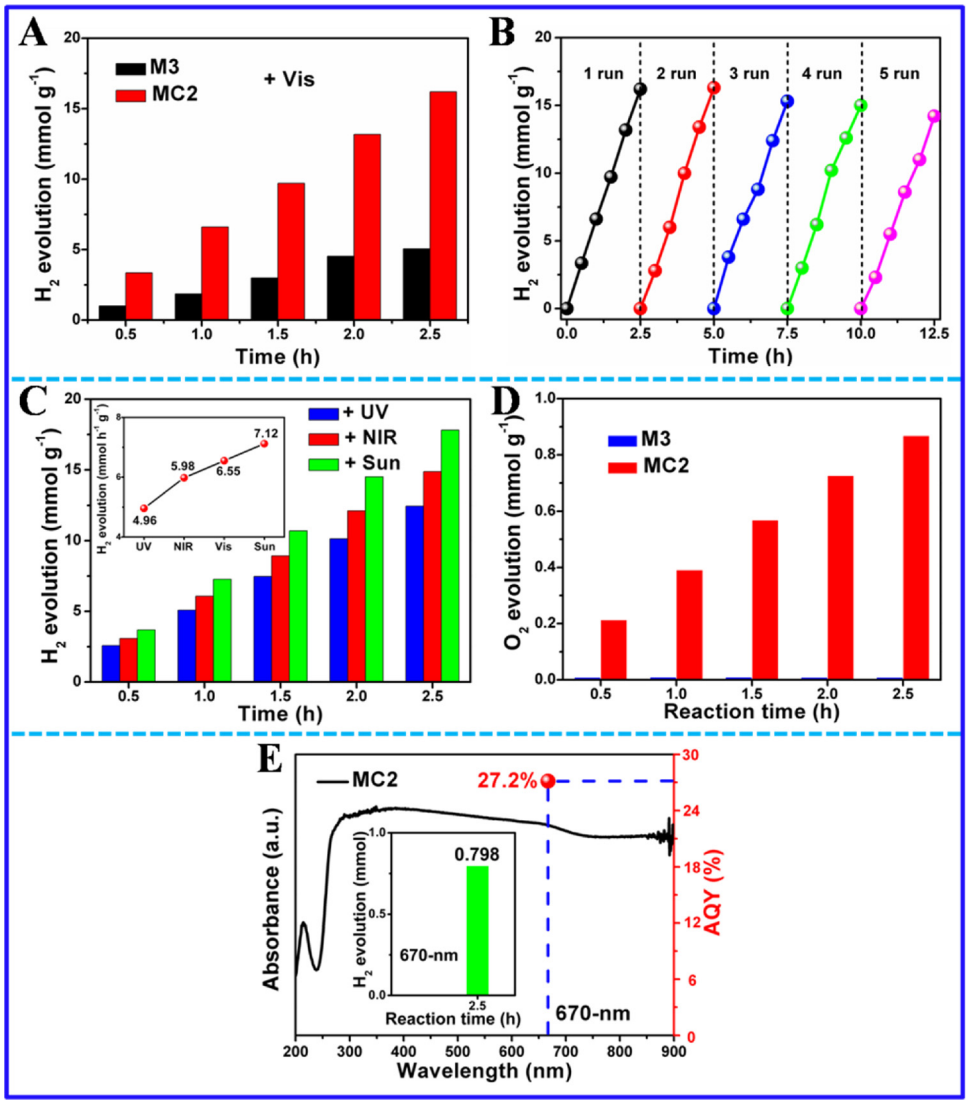

Fig. 9. (A) The H_2 production amount of M3 and MC2 with visible light irradiation. (B) Recycle runs of H_2 evolution over the MC2 sample under visible light irradiation. (C) The H_2 production amount of MC2 with different light sources irradiation. (D) The O_2 production amount of M3 and MC2 in Cr(VI) solution under stimulated sunlight irradiation. (E) Wavelength dependence of AQY (right axis) of the MC2 sample (50 mg) accompanied with its UV–vis absorption spectrum (left axis).

nanospheres (280 nm) also can be obtained by the same one-pot strategy. All the hollow spheres are assembled by many nanosheets, inducing the porous structure of the sample. Owing to the narrow band gap of $MoSe_2$ (1.53 eV) and CdSe (1.69 eV), the heterostructure possess great harvest in full spectrum. The energy band configuration was further surveyed by VB-XPS and DFT computation, showing the direct Z-scheme mechanism of $MoSe_2$/CdSe catalysts, which greatly improve the separation of photogenerated electron-hole and also remain the high oxidation and reduction capacity. The $MoSe_2$/CdSe heterostructure have a remarkable photocatalytic activity in degradation of Cr (VI) (125 mg g^{-1}, simulated sunlight), owing to the high absorption of full spectrum, hollow structure and separation of photo-generated electron and hole. The photocatalytic process was further studied in detail, showing that the Langmuir single-layer adsorption behavior, low pH value condition, and thermal effect also benefit to the high photoreduction performance. Benefiting from the Z-scheme mechanism, the high redox activity make sure the high water splitting capacity of MC2 (7120.0 and 348.0 μmol h^{-1} g^{-1} of H_2 and O_2 evolution) under simulated sunlight irradiation and its AQY for H_2 evolution at 670 nm reaches up to 27.2% (50 mg MC2). Finally, it is believed that the strategy used in this paper also can be expanded to other hollow $MoSe_2$ based heterostructure or other hollow selenides for the applications not only on photocatalysis but also on energy storage and conversion, biomedicine, and electrochemistry.

Acknowledgements

This work was supported by the National Natural Science Foundation of China (21471041, 21571045), College Youth Innovation Talents Training Program of Heilongjiang Province of China (UNPYSCT-2015053), and Outstanding Youth Science Fund of Harbin Normal University of China (XKYQ201404).

Appendix A. Supplementary data

Supplementary material related to this article can be found, in the online version, at doi:https://doi.org/10.1016/j.apcatb.2018.11.033.

References

[1] F. Wang, Y. Huang, Z. Chai, M. Zeng, Q. Li, Y. Wang, D. Xu, Chem. Sci. 7 (2016) 6887–6893.

[2] P.Y. Kuang, Y.Z. Su, K. Xiao, Z.Q. Liu, N. Li, H.J. Wang, J. Zhang, ACS Appl. Mater. Interfaces 7 (2015) 16387–16394.
[3] P.Y. Kuang, P.X. Zheng, Z.Q. Liu, J.L. Lei, H. Wu, N. Li, T.Y. Ma, Small 12 (2016) 6735–6744.
[4] R.-B. Wei, Z.-L. Huang, G.-H. Gu, Z. Wang, L. Zeng, Y. Chen, Z.-Q. Liu, Appl. Catal. B: Environ. 231 (2018) 101–107.
[5] Y. Yang, K. Shen, Y. Liu, Y. Tan, X. Zhao, J. Wu, X. Niu, F. Ran, Nano-Micro Lett. 9 (2016) 6.
[6] J. Kang, S. Tongay, J. Zhou, J. Li, J. Wu, Appl. Phys. Lett. 102 (2013) 012111.
[7] Y. Shi, C. Hua, B. Li, X. Fang, C. Yao, Y. Zhang, Y.-S. Hu, Z. Wang, L. Chen, D. Zhao, G.D. Stucky, Adv. Funct. Mater. 23 (2013) 1832–1838.
[8] R. Coehoorn, C. Haas, J. Dijkstra, C.J.F. Flipse, R.A. de Groot, A. Wold, Phys. Rev. B 35 (1987) 6195–6202.
[9] H. Chu, X. Liu, B. Liu, G. Zhu, W. Lei, H. Du, J. Liu, J. Li, C. Li, C. Sun, Sci. Rep. 6 (2016) 35304.
[10] H. Chu, W. Lei, X. Liu, J. Li, W. Zheng, G. Zhu, C. Li, L. Pan, C. Sun, Appl. Catal. A: Gen. 521 (2016) 19–25.
[11] H. Chu, W. Lei, X. Liu, J. Qu, J. Li, G. Zhu, L. Niu, L. Pan, J. Mater. Sci. Mater. Electron. 27 (2016) 5483–5489.
[12] U. Gupta, B.S. Naidu, U. Maitra, A. Singh, S.N. Shirodkar, U.V. Waghmare, C.N.R. Rao, Appl. Mater. 2 (2014) 092802.
[13] C. Dai, E. Qing, Y. Li, Z. Zhou, C. Yang, X. Tian, Y. Wang, Nanoscale 7 (2015) 19970–19976.
[14] L. Jia, X. Sun, Y. Jiang, S. Yu, C. Wang, Adv. Funct. Mater. 25 (2015) 1814–1820.
[15] D. Xie, W. Tang, Y. Wang, X. Xia, Y. Zhong, D. Zhou, D. Wang, X. Wang, J. Tu, Nano Res. 9 (2016) 1618–1629.
[16] G.D. Park, J.H. Kim, S.K. Park, Y.C. Kang, ACS Appl. Mater. Interfaces 9 (2017) 10673–10683.
[17] S. Yang, C. Shao, X. Li, X. Zhou, X. Li, J. Zhang, R. Tao, Y. Liu, J. Colloid Interface Sci. 518 (2018) 1–10.
[18] M. Wang, Z. Peng, J. Qian, H. Li, Z. Zhao, X. Fu, J. Hazard. Mater. 347 (2018) 403–411.
[19] B. Qu, X. Yu, Y. Chen, C. Zhu, C. Li, Z. Yin, X. Zhang, ACS Appl. Mater. Interfaces 7 (2015) 14170–14175.
[20] Z. Ren, X. Liu, H. Chu, H. Yu, Y. Xu, W. Zheng, W. Lei, P. Chen, J. Li, C. Li, J. Colloid Interface Sci. 488 (2017) 190–195.
[21] X. Zhou, Y. Liu, H. Ju, B. Pan, J. Zhu, T. Ding, C. Wang, Q. Yang, Chem. Mater. 28 (2016) 1838–1846.
[22] C. Huang, S. Wu, A.M. Sanchez, J.J. Peters, R. Beanland, J.S. Ross, P. Rivera, W. Yao, D.H. Cobden, X. Xu, Nat. Mater. 13 (2014) 1096–1101.
[23] D. Zeng, L. Xiao, W.J. Ong, P. Wu, H. Zheng, Y. Chen, D.L. Peng, ChemSusChem 10 (2017) 4624–4631.
[24] C.-F. Fu, Q. Luo, X. Li, J. Yang, J Mater. Chem. A 4 (2016) 18892–18898.
[25] S. Wei, Y. Song, Y. Rong, L. Tang, Y. Chen, C. Lu, Z. Zhang, J. Wang, Renew. Energy 111 (2017) 628–637.
[26] Z.-F. Huang, J. Song, X. Wang, L. Pan, K. Li, X. Zhang, L. Wang, J.-J. Zou, Nano Energy 40 (2017) 308–316.
[27] J. Low, C. Jiang, B. Cheng, S. Wageh, A.A. Al-Ghamdi, J. Yu, Small Methods 1 (2017) 1700080.
[28] F. Xu, W. Xiao, B. Cheng, J. Yu, Int. J. Hydrogen Energy 39 (2014) 15394–15402.
[29] Y. Song, S. Wei, Y. Rong, C. Lu, Y. Chen, J. Wang, Z. Zhang, Int. J. Hydrogen Energy 41 (2016) 12826–12835.
[30] D. Zeng, P. Wu, W.-J. Ong, B. Tang, M. Wu, H. Zheng, Y. Chen, D.-L. Peng, Appl. Catal. B: Environ. 233 (2018) 26–34.
[31] S. Kou, X. Guo, X. Xu, J. Yang, Catal. Commun. 106 (2018) 60–63.
[32] M.B. Tahir, G. Nabi, T. Iqbal, M. Sagir, M. Rafique, Ceram. Int. 44 (2018) 6686–6690.
[33] G. Wang, X. Ma, C. Wang, S. Li, J. Qiao, H. Zhang, G. Li, J. Wang, Y. Song, J. Mol. Liq. 260 (2018) 375–385.
[34] J. Chen, X.J. Wu, Y. Gong, Y. Zhu, Z. Yang, B. Li, Q. Lu, Y. Yu, S. Han, Z. Zhang, Y. Zong, Y. Han, L. Gu, H. Zhang, J. Am. Chem. Soc. 139 (2017) 8653–8660.
[35] D. Kong, H. Wang, J.J. Cha, M. Pasta, K.J. Koski, J. Yao, Y. Cui, Nano Lett. 13 (2013) 1341–1347.
[36] J.S. Rhyee, J. Kwon, P. Dak, J.H. Kim, S.M. Kim, J. Park, Y.K. Hong, W.G. Song, I. Omkaram, M.A. Alam, S. Kim, Adv. Mater. 28 (2016) 2316–2321.
[37] J.C. Shaw, H. Zhou, Y. Chen, N.O. Weiss, Y. Liu, Y. Huang, X. Duan, Nano Res. 7 (2015) 511–517.
[38] J. Xia, X. Huang, L.Z. Liu, M. Wang, L. Wang, B. Huang, D.D. Zhu, J.J. Li, C.Z. Gu, X.M. Meng, Nanoscale 6 (2014) 8949–8955.
[39] X. Wang, Y. Gong, G. Shi, W.L. Chow, K. Keyshar, G. Ye, R. Vajtai, J. Lou, Z. Liu, E. Ringe, B.K. Tay, P.M. Ajayan, ACS Nano 8 (2014) 5125–5131.
[40] H.J. Fan, U. Gosele, M. Zacharias, Small 3 (2007) 1660–1671.
[41] Y. Yin, R.M. Rioux, C.K. Erdonmez, S. Hughes, G.A. Somorjai, A.P. Alivisatos, Science 304 (2004) 711–714.
[42] N. Li, J. Wu, Y. Lu, Z. Zhao, H. Zhang, X. Li, Y.-Z. Zheng, X. Tao, Appl. Catal. B: Environ. 238 (2018) 27–37.
[43] Y. Qu, H. Medina, S.W. Wang, Y.C. Wang, C.W. Chen, T.Y. Su, A. Manikandan, K. Wang, Y.C. Shih, J.W. Chang, H.C. Kuo, C.Y. Lee, S.Y. Lu, G. Shen, Z.M. Wang, Y.L. Chueh, Adv. Mater. 28 (2016) 9831–9838.
[44] M.-H. Wu, J.-T. Lee, Y.J. Chung, M. Srinivaas, J.-M. Wu, Nano Energy 40 (2017) 369–375.
[45] J. Xu, X. Cao, Chem. Eng. J. 260 (2015) 642–648.
[46] L. Shen, W. Wu, R. Liang, R. Lin, L. Wu, Nanoscale 5 (2013) 9374–9382.
[47] Z. Lei, W. Zhu, S. Xu, J. Ding, J. Wan, P. Wu, ACS Appl. Mater. Interfaces 8 (2016) 20900–20908.
[48] Y. Wang, F. Zhang, Q. Wang, P. Yang, H. Lin, F. Qu, Nanoscale 10 (2018) 14534–14545.
[49] L. Yuwen, J. Zhou, Y. Zhang, Q. Zhang, J. Shan, Z. Luo, L. Weng, Z. Teng, L. Wang, Nanoscale 8 (2016) 2720–2726.
[50] J. Jia, H. Wang, Z. Lu, P.G. O'Brien, M. Ghoussoub, P. Duchesne, Z. Zheng, P. Li, Q. Qiao, L. Wang, A. Gu, A.A. Jelle, Y. Dong, Q. Wang, K.K. Ghuman, T. Wood, C. Qian, Y. Shao, C. Qiu, M. Ye, Y. Zhu, Z.-H. Lu, P. Zhang, A.S. Helmy, C.V. Singh, N.P. Kherani, D.D. Perovic, G.A. Ozin, Adv. Sci. 4 (2017) 1700252.
[51] B. Mao, T. Bao, J. Yu, L. Zheng, J. Qin, W. Yin, M. Cao, Nano Res. 10 (2017) 2667–2682.
[52] X. Zhang, X. Li, M.E. Reish, D. Zhang, N.Q. Su, Y. Gutiérrez, F. Moreno, W. Yang, H.O. Everitt, J. Liu, Nano Lett. 18 (2018) 1714–1723.
[53] Z. Zhang, J. Huang, Y. Fang, M. Zhang, K. Liu, B. Dong, Adv. Mater. 29 (2017) 1606688.
[54] S. Ma, Y. Deng, J. Xie, K. He, W. Liu, X. Chen, X. Li, Appl. Catal. B: Environ. 227 (2018) 218–228.
[55] D. Zhong, W. Liu, P. Tan, A. Zhu, Y. Liu, X. Xiong, J. Pan, Appl. Catal. B: Environ. 227 (2018) 1–12.
[56] K. He, J. Xie, X. Luo, J. Wen, S. Ma, X. Li, Y. Fang, X. Zhang, Chin. J. Catal. 38 (2017) 240–252.
[57] D. Jiang, L. Zhu, R.M. Irfan, L. Zhang, P. Du, Chin. J. Catal. 38 (2017) 2102–2109.
[58] S. Ma, X. Xu, J. Xie, X. Li, Chin. J. Catal. 38 (2017) 1970–1980.
[59] P. Wang, Y. Sheng, F. Wang, H. Yu, Appl. Catal. B: Environ. 220 (2018) 561–569.
[60] Z. Yue, A. Liu, C. Zhang, J. Huang, M. Zhu, Y. Du, P. Yang, Appl. Catal. B: Environ. 201 (2017) 202–210.
[61] W. Yu, D. Xu, T. Peng, J. Mater. Chem. A 3 (2015) 19936–19947.
[62] Y. Peng, Z. Guo, J. Yang, D. Wang, W. Yuan, J. Mater. Chem. A 2 (2014) 6296–6300.
[63] K. Song, F. Xiao, L. Zhang, F. Yue, X. Liang, J. Wang, X. Su, J. Mol. Catal. A: Chem. 418–419 (2016) 95–102.
[64] H. Gao, P. Zhang, J. Zhao, Y. Zhang, J. Hu, G. Shao, Appl. Catal. B: Environ. 210 (2017) 297–305.
[65] Q. Jia, A. Iwase, A. Kudo, Chem. Sci. 5 (2014) 1513.
[66] A. Rauf, M. Ma, S. Kim, M.S.A. Sher Shah, C.-H. Chung, J.H. Park, P.J. Yoo, Nanoscale 10 (2018) 3026–3036.
[67] K. Kailasam, A. Fischer, G. Zhang, J. Zhang, M. Schwarze, M. Schröder, X. Wang, R. Schomäcker, A. Thomas, ChemSusChem 8 (2015) 1404–1410.
[68] M. Zhu, Z. Sun, M. Fujitsuka, T. Majima, Angew. Chem. Int. Ed. 57 (2018) 2160–2164.
[69] J. Liu, Y. Liu, N. Liu, Y. Han, X. Zhang, H. Huang, Y. Lifshitz, S.-T. Lee, J. Zhong, Z. Kang, Science 347 (2015) 970–974.
[70] W. Jiang, S. Bai, L. Wang, X. Wang, L. Yang, Y. Li, D. Liu, X. Wang, Z. Li, J. Jiang, Y. Xiong, Small 12 (2016) 1640–1648.
[71] Y. Li, M. Yang, Y. Xing, X. Liu, Y. Yang, X. Wang, S. Song, Small 13 (2017) 1701552.
[72] X. Shi, M. Fujitsuka, S. Kim, T. Majima, Small 14 (2018) e1703277.
[73] M. Xing, J. Zhang, B. Qiu, B. Tian, M. Anpo, M. Che, Small 11 (2015) 1920–1929.
[74] G. Liu, J. Pan, L. Yin, J.T.S. Irvine, F. Li, J. Tan, P. Wormald, H.-M. Cheng, Adv. Funct. Mater. 22 (2012) 3233–3238.
[75] A. Primo, A. Corma, H. Garcia, Phys. Chem. Chem. Phys. 13 (2011) 886–910.
[76] B. Wang, S. Shen, L. Guo, Appl. Catal. B: Environ. 166–167 (2015) 320–326.
[77] X. Yin, X. Li, H. Liu, W. Gu, W. Zou, L. Zhu, Z. Fu, Y. Lu, Nano Energy 49 (2018) 489–497.
[78] H. Ou, L. Lin, Y. Zheng, P. Yang, Y. Fang, X. Wang, Adv. Mater. 29 (2017) 1700008.